

Steve Cochard · Christophe Ancey

Tracking the free surface of time-dependent flows: Image processing for the dam-break problem

Received: date / Accepted: date

Abstract The dam-break problem (i.e., the sudden release of a given volume of fluid down a slope) has attracted much attention from mechanicians and physicists over the last years. Of particular interest are the free-surface profile and the spreading rate. Experimentally, impediments to accurate measurements of the free-surface evolution are numerous because of the significant variations in its curvature and velocity.

In order to accurately measure the free-surface variations with time of a surge, we developed a new imaging system. This system consists in a digital camera coupled with a synchronised micro-mirrors projector. The object surface is imaged into a camera and patterns are projected onto the surface under an angle of incidence that differs from the imaging direction. From the deformed pattern recorded by the camera, phase can be extracted and, by using unwrapping algorithms, height can be computed and the free surface is reconstructed. We measure the free surface of the flow to within 0.1 mm over a surface of $1.8 \times 1.1 \text{ m}^2$.

Keywords Free surface · dam-break problem · surface reconstruction · image processing

1 Introduction

Shallow-water equations have been originally worked out by Saint Venant (1871) to compute flood propagation along rivers. Their use was gradually extended to strongly time-dependent flows such as waves induced by a dam break (Ritter, 1892). There is currently a growing number of models based on the shallow-water equations, which are used to describe natural flows such as flash floods (Hogg and Pritchard, 2004), floods with sediment transport (Pritchard, 2005), snow avalanches (Bartelt et al, 1999), debris flows (Iverson, 1997; Huang and Garcia, 1997), lava flows (Griffiths, 2000), subaqueous avalanches (Parker et al, 1986), etc. In the derivation of these models, a number of assumptions are used, the most important of which are: the long-wave approximation (no significant curvature of the free surface), hydrostatic pressure, blunt velocity profile, and no change in the bulk composition or rheology. Furthermore, in these models, the bottom shear stress is computed using either empirical expressions (e.g., Chézy friction) or non-Newtonian constitutive equations, with the difficult question of parameter fitting. Given the number of approximations and assumptions needed for obtaining these models, one can be legitimately be suspicious about their reliability and performance.

Essentially, our idea was to test the shallow-flow equations under extreme conditions in a well controlled environment—the laboratory—, where both the initial and boundary conditions are prescribed. Here, ‘extreme conditions’ mean that we focus our attention on time-dependent flows (surges with a front) mobilizing non-Newtonian fluids, experiencing different stages from release to run-out: acceleration (balance between inertia and pressure gradient), nearly fully developed regime (flow at equilibrium), and deposition (prevalence of dissipation processes). Preliminary experiments are run with viscoplastic materials.

The objective of this paper is to describe the experimental procedures used for reconstructing three-

Steve Cochard
Ecole Polytechnique Fédérale de Lausanne
EPFL - ENAC - ICARE - LHE
Station 18 / GC A1-391
CH - 1015 Lausanne
Switzerland
Tel.: +41 21 693 59 16
E-mail: steve.cochard@epfl.ch

Christophe Ancey
E-mail: christophe.ancey@epfl.ch

dimensional, time-dependent profiles of flow depth. To give the reader an overview of the experimental setting, we will describe the experimental facilities and procedures that we used to generate surges down an inclined plane (see Sect. 2). Tracking the free surface of a rapid surge remains delicate, especially when fastness and accuracy are sought. Various techniques have been used in recent years. For instance, Iverson et al (2004) used parallel laser sheets to reconstruct of rapid granular avalanches down irregular topography; ? used a Moiré technique for the same purpose. Here, we will present an image-processing technique based on pattern projection. In itself, the technique is not new (Desmangles, 2003, e.g., see), but we think that our particular application is innovative given the number of technical problems that must be sorted out to operate it in dam-break experiments. Various strategies can be contemplated to reconstruct three-dimensional, time-dependent free surfaces, as reviewed in Sect. 3.1. Pattern projection turns to be very convenient in terms of cost, robustness, accuracy, and versatility. A key point concerns the back computation of flow depth. In Sect. 3.2 and 3.3, we will show how to use fringe deformation to reconstruct a three-dimensional profile. The basic idea underpinning our developments is that in terms of signal processing, free-surface variations entail fringe deformations, viz phase shift and, possibly, amplitude modulation. Section 4 is devoted to phase mapping; the different algorithms used will be outlined there. Usually, a phase map was calculated using a 3/4-image algorithm (as described in Sect. 4.1); for fast flows, we used a one-image algorithm (see Sect. 4.2 and 4.3). Back computation (recovering flow depth from phase shift) will be presented in Sect. 5: the flow depth is merely deduced by unwrapping the phase signal (see Sect. 5). This phase unwrapping involves a calibration procedure, which is described in Sect. 5.2. Eventually, we will yield an example of application in Sect. 6.

2 Facility and procedures

2.1 Overview

Figure 1 gives an outlook of the experimental setup, while Fig. 2 shows the upper inclined plane, the reservoir, and the gate. Typically, an experiment is run as follows. An amount of fluid is placed in a reservoir at the top of an inclined plane. The fluid is suddenly released by opening the dam's sluice gate. Using a high-speed digital camera, we then record how a fringe pattern projected on the flow surface is deformed, which makes it possible to measure the flow depth at any place on the surface.

More specifically, our system worked in the following way. A micro-mirror projector projected periodic fringe patterns of incoherent light onto the surface, as

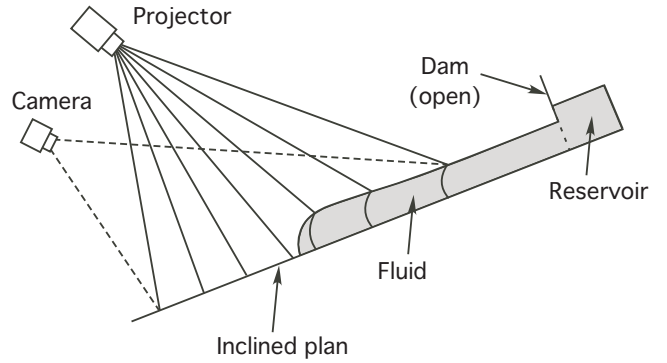


Fig. 1 Sketch showing the experimental setup and the measurement system.



Fig. 2 View on the sluice gate and the reservoir at the channel inlet.

explained in Sect. ???. We placed the digital camera above the flow, but with an incidence angle that differed from the projection angle. This camera recorded how the projected fringes were deformed by the free surface. In terms of signal processing, fringe deformation is equivalent to a phase offset, which can be shown to be directly proportional to the local flow thickness. Thus, measuring flow depth boils down to measuring phase offset.

2.2 Experimental facility

The facility is made up of a metallic frame supporting an inclined plane, horizontal plane (run-out zone), and reservoir, as sketched in Fig. 3. This structure is 6 m long, 1.8 m wide, and 3.5 m high. The 4.5-m long aluminium inclined plane can be inclined from 0° to 45° by the means of an electrical engine. Its position is accurately imposed using a laser-meter to within 1 mm, which means that the accuracy of slope inclination is of the order of 10^{-2}° . The 6-mm thick aluminium plate is supported by a frame made up of profiled aluminium beams (of section $40 \times 80 \text{ mm}^2$), which ensure rigidity.

Different PVC channels can be positioned on the inclined plane in order to limit the spreading of the fluid along the cross-stream direction. As the inclined plane, the channels can be inclined from 0° to 45° and can have different width and shape.

A PVC reservoir of varying volume and shape is positioned at the top of the inclined plane behind the dam wall. The maximum capacity of the reservoir is 120 kg. The dam wall is composed of a 1.6×0.8 m² ultralight carbon plate. The 35-cm high sluice gate is opened within 0.8 s by two pneumatic jacks on each side. Using ultralight dam wall was needed to reduce dam-wall inertia, induced vibration, and jerk. The two jacks are fast rose by injecting air pressured at 7 mPa. Two electromagnetic sensors were located at the tip of each jack to control its position and reset the clock.

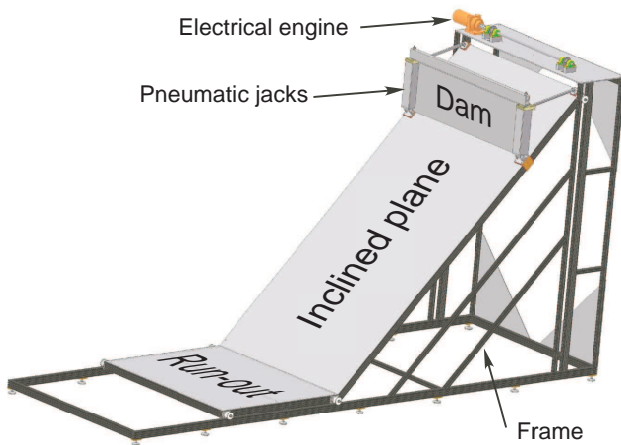


Fig. 3 Schematic perspective of the facility.

The run-out plane has two functions: first, it collects the fluid flowing from the inclined plane, which makes the cleaning operations easier. Second—and this is the most important point—the flowing material is forced to experience a transition from a flow regime to a deposition (run-out) regime. The 1.5-m long, 1.8 m-wide run-out plane is maintained in a horizontal position and is connected to the inclined plane by a sealing plastic band. The projector and the camera are fixed on another frame, which is independent of the main frame.

2.3 Experimental procedure

A typical experimental run can be split into four stages.

1. The fluid is prepared in advance (i.e., one or two days) and stocked in a 60-l drum. The viscoplastic fluid used so far is a stable polymeric gel (Carbopol Ultrez 10 provided by Gattefossé AG, Luzern, Switzerland). Polymer chains are vigorously mixed into a sodium-hydroxide/water solution at a given

pH. This blend is left at rest for a long time so that all polymer chains have time to unroll and form a dispersion (repulsive interactions between chains). To ensure good light contrast, Titanium Dioxide (TiO_2) is added to whiten Carbopol.

2. The fluid is gently poured into the reservoir, while the inclined plane is kept in horizontal position. The material is then slowly mixed and its free surface is smoothed out by hand. The upper plane is then inclined at a given value and its position is checked using a laser-meter. A viscoplastic fluid does not flow if shear stresses are too low, which means that its free surface stays in the reservoir as it stood after pouring; there is no stress relaxation (due to viscoelasticity), nor creeping (due to viscosity), which would cause flattening of the free surface, which explains why the free surface remains parallel to the plane and needs being smoothing before we unleash it.
3. Once all the devices are installed, the measurement system is calibrated, as explained at length in Sect. 5.2. A few minutes before starting the test, we collect a fluid sample and test it using a Bohlin CVOR rheometer to characterize its rheological properties.
4. We lift up the sluice gate and the material starts accelerating and flowing. The surge motion is followed up by the digital camera. When there is no significant motion, we stop to record images. The material is then removed from the flume and the plane is carefully cleaned out.

3 Measurement system

3.1 How to measure the free-surface variations with time?

For dam-break experiments, the crux of the difficulty lies in the proper measurement of the free-surface evolution. We thought of different systems. Three criteria guided our choice. First, we needed a non-invasive system to avoid disturbing the free boundary. Second, our preference was on global methods that are able to capture the flow surface within a single pass in contrast with scanning methods, which are not well suited to providing snapshots. Third, we wished to develop a method, which enables high acquisition rates.

Three global systems were considered:

1. A method, which involves projecting patterns onto the fluid surface. Pattern deformation is recorded by a camera. This method is described in section 3.2.
2. A stereoscopic system, with two cameras scrutinizing the same surface. This method performs well with surfaces of varying color and contrast since colored pixels can be used as reference points and tracked (Kraus and Waldhäusl, 1997). The height is

computed by taking the difference between two successive images recorded by the two cameras. Since our fluids are monochromatic, this method has been discarded.

3. A system based on the time of fly of emitted photons. Photons are emitted by a source, a number of which are back-scattered by the surface. The time between their emission and reception provides an estimate of the travelled distance (Niclass et al, 2005). This method performs well solely for static objects, but should be a promising technique for our purpose in the forthcoming years.

3.2 Projecting patterns

Measuring the shape of an object using the pattern projection can be broken down into three steps:

1. a given pattern is projected onto an object;
2. the object surface is imaged into a camera under an angle of incidence that differs from the imaging direction; and
3. the surface height is retrieved from the image.

For the sake of simplicity, two parallel lines are projected onto a surface, as shown in Fig. 4 (?). The height difference Δh can be then expressed as

$$\Delta h = \frac{\Delta p}{\tan \alpha}, \quad (1)$$

where $\Delta p = p_p - p_a$ is the difference between p_p the projected lines onto the object and p_a the apparent line on the surface viewed by the camera; α is the angle between the projected lines and the camera.

This simple relationship emphasizes two points. First, the closer the projected lines p_p are, the greater the accuracy of Δh is. Second, the closer to 90° the angle α is, the better the accuracy of Δh is.

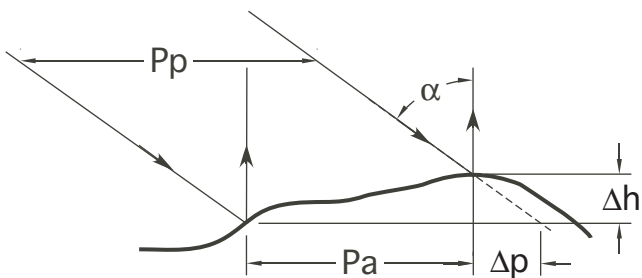


Fig. 4 Projection of parallel lines on a surface and the retrieved height.

A problem with projecting lines is that any valuable information between two lines is lost, as illustrated by Fig. 5. There is another technical problem related to the camera resolution: for two lines to be distinguished by the camera, there must be a minimum distance of three

pixels, which imposes a lower bound on the accuracy of Δh according to equation (1).

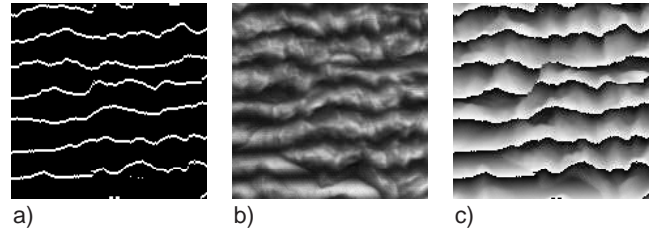


Fig. 5 Comparison between: a) projection of lines, b) projection of fringes and c) the resulting phase map.

Another problem stems from computing the difference Δp when it becomes larger than one half of the projected line P_p since in that case, it is no longer associated with the closest reference line. This result in a negative value Δh , whereas a large positive one is expected. Fig. 6 illustrate this loss of information: island 2 is embedded into Island 1 and there is no convenient way of determining whether Island 2 is located above or below Island 1.

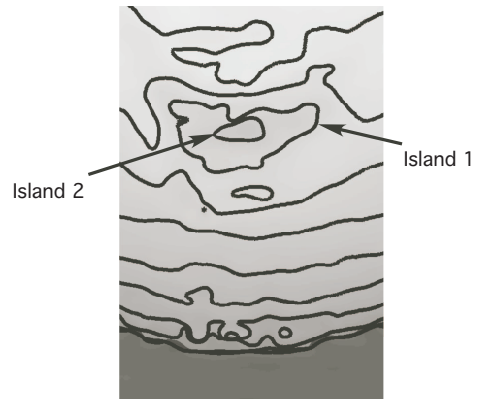


Fig. 6 Loss of information due to looped line or islands. Is Island 2 at higher or lower elevation than Island 1?

3.3 Projecting fringes

Instead of isolated lines, we can project cosine fringe patterns. Information theory would say that we replace a 2 bit system into an 8 bit system, which should enhance accuracy and robustness. Moreover, instead of relating height with light intensity, we can link height to fringe phase. The observed intensity at a given point (x, y) can be written as

$$I_k(x, y) = A_k(x, y) + B_k(x, y) \cos \phi_k(x, y), \quad (2)$$

where A_k and B_k represent the background and the modulation intensities and ϕ_k denotes the phase. The phase varies within the interval $[0, 2\pi)$. Working with phase instead of intensity has the substantial advantage that alteration in surface reflectivity does not influence the outcome.

We used an imaging system, which consists of a digital camera coupled with a synchronized micro-mirror projector working at a maximum rate of 48 Hz. The 1000×1000 px CCD camera and the projector are synchronized by the frame grabber. The actual projection surface is 1.8×1.1 m². The main advantage of a micro-mirror projector (MMD) lies in its capacity to instantaneously project a given pattern. As mentioned in Sect. 3.1, achieving high resolution in time and space requires global acquisition and projection. Compared to a laser interferometer, projecting fringe patterns with a MMD has also the advantage of versatility and safety. There is, however, a price to pay when using a MMD instead of a laser interferometer: we have to use non-coherent light, which implies lower intensity. Even in poor light conditions, the technique can perform fairly well since it can use a narrow range of 30 gray values; recall that perfect grabbed images taken by a 8 bit camera are characterized by an intensity range from 0 (deep black) to 255 (white).

The projector is made up micro-mirrors 1024×768 which oscillate between two positions and onto which light is projected from a led; for one position, light is reflected through the projector lens, while for the other position, light is not reflected. It is a binary system: for a given pixel, light is switched on or off. A 8-bit grey level is achieved thus by changing the projection duration of each micro-mirror.

At its maximum rate, the camera records an image within 20.7 ms, while the fringes are projected for 20.3 ms. A time lag of 0.1 ms separates two images. Special attention was paid to insuring that projection occurs entirely during the acquisition time and there is no synchronization delay. This would have no consequence with projection continuously operating with time (as with laser interferometry) but, as the MMD is originally a 2-bit projection system, relative intensity is controlled by the projection duration and this any error (e.g., error due to time discretization) may lead to significant errors in the post-treatment of images.

Capturing 48 images per second with a 1000×1000 px camera (i.e. 48 Mbytes/s) during time intervals as long as 10 minutes requires a CameraLink connection between the camera and the frame grabber. To store a huge amount of data within short intervals of time, we have implemented 4 hard disks in parallel into a RAID-0 system. Note that the acquisition program has been entirely developed using LabView.

4 Phase mapping

The phase map is a graphical representation (density plot) of the $\phi_k(x, y)$ functions [see Eq. (2)]. Optic convention is used here: high values (2π) are in white, whereas lower values (0) are in black.

Most algorithms used for retrieving phase from an image or a series of images use one the following method: phase-shifting Fourier transform (Takeda et al, 1982), local wave retrieval (Liebling et al, 2004), or wavelets. The three first methods are outlined in Sect. 4.1, 4.2 and 4.3, respectively. The phase map is also often referred to as the *wrapped phase*, which explains why we speak of unwrapping techniques when recovering flow depth from phase shift.

Note that to enhance accuracy, we must adapt our unwrapping algorithm with respect to the fluid velocity. In the earlier times of a run (typically 1–2 s), the flows accelerate vigorously and a one-image algorithm is used. After the flow has sufficiently slowed down, a 3- or 4-image algorithm is used.

Note also that for the phase map to be retrieved from the grabbed image(s), the images should not be saturated. If the grabbed images contain saturated pixels the result is a loss of information and the creation of additional frequencies in the phase map.

4.1 Phase shifting

Its principle consists in projecting $N \geq 3$ images of a fringe pattern shifted by $(i - 1)2\pi/N$, with $i = 1 \dots N$ (Desmangles, 2003). The phase can be analytically computed from the series of images. An example with a series of $N = 4$ images is given in Fig. 7, with the following intensities

$$\begin{cases} I_1(x, y) = A + B \cos \phi(x, y), \\ I_2(x, y) = A + B \cos(\phi(x, y) + \frac{\pi}{2}), \\ I_3(x, y) = A + B \cos(\phi(x, y) + \pi), \\ I_4(x, y) = A + B \cos(\phi(x, y) + \frac{3\pi}{2}), \end{cases}$$

where

$$\phi = f(I_1, I_2, I_3, I_4) = \arctan \frac{I_4 - I_2}{I_1 - I_3}. \quad (3)$$

The phase map resulting from this method is accurate since it results from analytical calculation. A phase map can be extracted with each new image using the $N - 1$ preceding ones.

Three-fringe patterns can be projected at the same time using a red-green-blue (RGB) color coding. An independent phase map can be extracted with each new image. The idea is attractive, but requires a complicated and expensive setting (Jeong and Kim, 2002).

The method based on 3 or 4 images is more appropriate when the fluid slows down and the relative motion between the first and the last images is less than

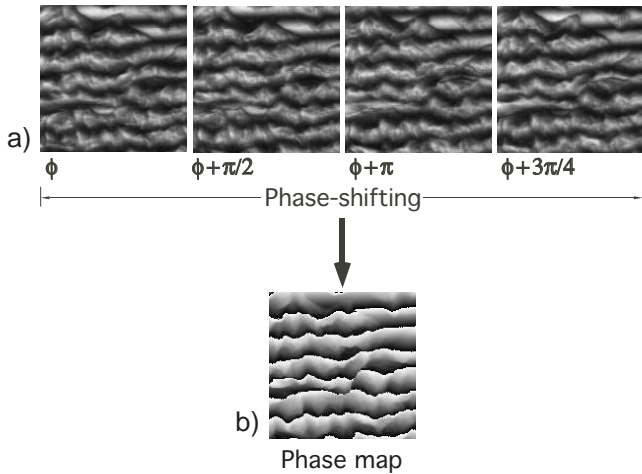


Fig. 7 Phase shifting: a) with 4 images and b) the resulting phase map.

a 1 or 2 pixels. This method is not suitable at earlier times, when the fluid is released because the displacement of the fluid between the first and the last images is too large. The resulting phase map is blurred and unusable. During the first instants of the test, the phase map must be computed with just one image; this computation can be done with a FFT algorithm, as explained in Sect. 4.2, or with a local wave retrieval algorithm, as described in Sect. 4.3.

4.2 Fourier transformation profilometry (FTP)

Fourier transformation profilometry (FTP) was first introduced by Takeda et al (1982). The idea is to work in the frequency domain of the recorded images in order to filter out the signal and keep only the desired frequencies (Sansoni et al, 1999).

In this subsection, we shall not explain how FTP works, but just provide some ideas on how we have implemented FTP in our setup. A cosine fringe pattern with 45° inclinations is projected onto the surface of the reference plane during the calibration procedure, as shown in Fig. 8(a) (see also Sect. 5.2). Two-dimensional Fourier transform analysis is then carried out on the recorded images as follows:

1. the central peak representing frequencies close to zero is removed;
2. the frequency F_ϕ of the cosine fringe projected is localized [see Fig. 8(b)];
3. the frequency map is filtered out to keep only the desired values [see Fig. 8(c)];
4. the frequency map is shifted from the frequency F_ϕ to the center $F = 0$ [see Fig. 8 (c)]; and
5. the angle of the inverse FFT is computed, which provides us with the phase map of the reference plane [see Fig. 8(d)].

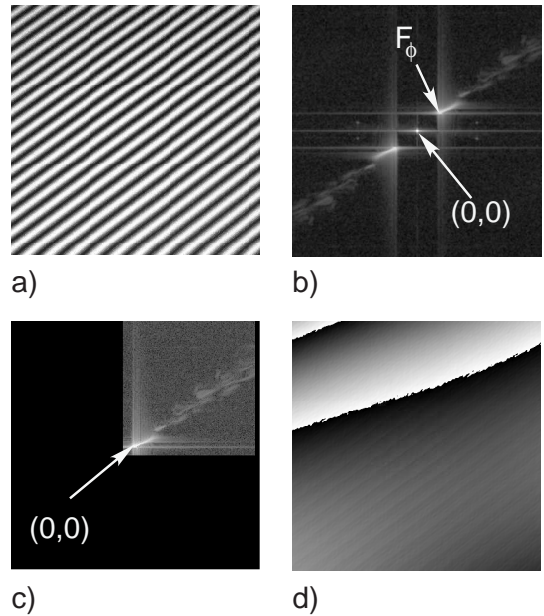


Fig. 8 Reference plane: a) projected fringes, b) image in FFT domain with the frequency F_ϕ of the projected fringe, c) image filtered and shifted and d) reference plane phase map.

The same procedure is then repeated, during the test, with the recorded images except that the frequency map is shifted by the value F_ϕ , which was computed during the calibration procedure. Figure 9 shows a typical example, with can be compared with the images obtained when using the reference plane (Fig. 8). The wrapped phase is then obtained by subtracting the new phase and the phase of the reference plane [see Fig. 9 (d)]. The resulting phase is the difference between the object phase and the reference-plane phase. Section 5.1 will show that unwrapping the difference between the object-phase and reference-phase maps is equivalent to the difference of the unwrapped phases.

FTP can be improved by removing image modulation so that the central peak of frequencies close to zero in the frequency map (related to the plane) is eliminated. This is achieved during the calibration procedure by shifting $N \geq 3$ fringe patterns by $(i-1)2\pi/N$ with $i = 1 \dots N$, as explained in section 4.1. The modified image is then

$$I = I_1 - \frac{1}{N} \sum_{n=1}^N I_n.$$

FTP performs much better when the frequency of the projected cosine fringe is high and fringes are inclined at 45° with respect to in the recorded image. In the frequency map, frequency F_ϕ is moved away from the origin 0 (by a factor of $\sqrt{2}$ in comparison with a projection of fringes at 0°), filtering and shifting are more accurate. The drawback of a 45° projection is that the relative projected line P_p viewed by the camera is

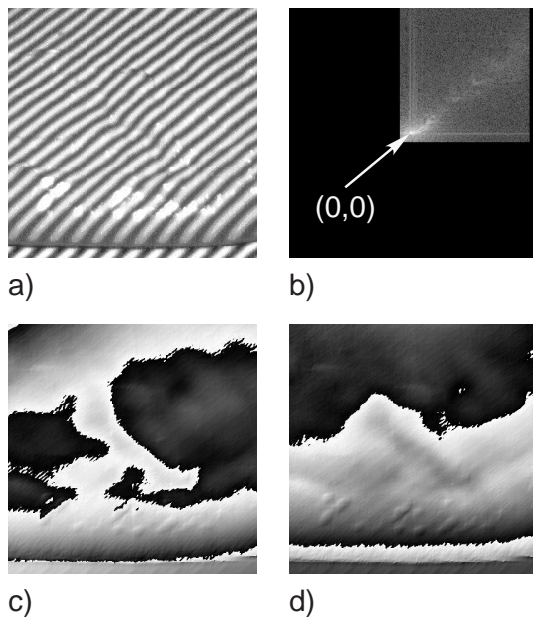


Fig. 9 Object: a) projected fringes, b) object image filtered and shifted in Fourier domain c) resulting phase map and d) difference between the object phase map and the reference plane phase map.

increased by a factor of $\sqrt{2}$, which results in a lower accuracy of the measurement [see Eq. (1)].

Su and Chen (2001) discussed the influence of sampling in FTP. They emphasized that the recorded images as well as discrete Fourier Transform (DFT) are digital, whereas FTP theory is based on continuous Fourier transform. This difference between theory and experimental treatment induces errors at high frequencies values. We are working to implement methods for reducing errors that arise at high frequencies; note that this issue remains of secondary importance in our context since our flows involve low frequencies most of the time.

FTP efficiency depends a great deal on filtering, i.e., how many frequencies must be kept or not. An experienced user can easily find frequencies that must be removed in order to enhance map accuracy. Making this process automatic is, however, quite difficult. It is almost impossible to know in advance when a phase-shifting algorithm can be used as a replacement for FTP. To overcome this issue, we project 45° -inclined fringes with a phase shift of $2(i-1)\pi/N$, with $i = 1 \dots N$. Both phase-shifting and FTP algorithms can then be used depending on the quality of their respective phase map.

As illustrated through Fig. 10(a), this method encounters serious problems when the projection pattern is parallel to a shadow region. In this case, there is no real possibility to differentiate dark area due to shadow from dark area due to the projection. Wrong frequencies are introduced, which result in an incorrect wrapped

phase, as highlighted in Fig. 10(b). On the opposite, if the light pattern crosses the shadow area perpendicularly, the wrapped phase remain of fair quality, except that all pieces of information contained in a shadow region are lost (see Sect. 5). If the image were symmetric, one way to get round this problem would be to cut the image into two identical parts, remove one half, and keep the other. This technique is delicate because there is no possibility to check whether the flow is really symmetric, as assumed, or not. Each symmetric part of the flow could be treated independently with a symmetric projection, as shown in Fig. 12(a). FTP method cannot deal with multiple projection direction because many frequencies F_ϕ then arise in the frequency map, while a single one is desired. Each image has to be divided into two halves with respect the center of symmetry. In practice, this procedure is hardly feasible because it involves carefully aligning the camera, the projector, and the inclined-plane axis. That is why we used FTP solely when we want to have a close-up on a given region.

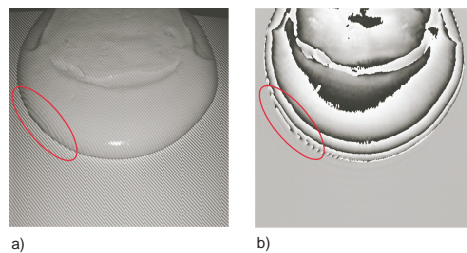


Fig. 10 Fringe projection at 45° : a) grabbed image, b) phase map computed with FTP. The phase map exhibits wrong frequencies on the bottom left corner (area marked with the ellipsis).

In a non-telecentric setup (see Sect. 5.2), the fringe frequency changes with the incidence angle of the camera. Frequency F_ϕ is no longer represented by a sharp peak in the frequency map, but by something a bit more diffuse, as illustrated in Fig. 11.

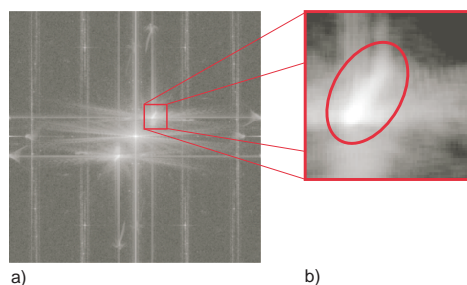


Fig. 11 Image in the FFT domain with the frequency F_ϕ of the projected fringe in a non-telecentric setup: a) overview, b) close-up of the diffuse peak F_ϕ

4.3 Local wave retrieval

Different methods have been so far developed to retrieve the phase of a signal, using one image and local algorithm. We have decided to work with Liebling's algorithm (Liebling et al, 2004).

In local wave retrieval methods, one assumes that locally, only the value of the phase ϕ_k changes, while the background and modulation intensities A_k and B_k stay constant. The basic idea is then to divide an image into small windows and estimate the phase on each of those windows by assuming that, in a given window, only the phase ϕ changes. The phase is retrieved by interpolating with cubic spline functions. Empirically, one observes that results are improved when small phase steps and window of sizes ranging from two to four phase steps are used.

As for FTP, Liebling's algorithm requires a reference image to calculate the phase ϕ of the object. Any projected image could be used as far as its frequency is high. Again, to circumvent the problem of shadow regions, we use the same technique as that explained in Sect. ???. As for FTP, the resulting phase map is defined as the difference between the object-phase and reference-phase map.

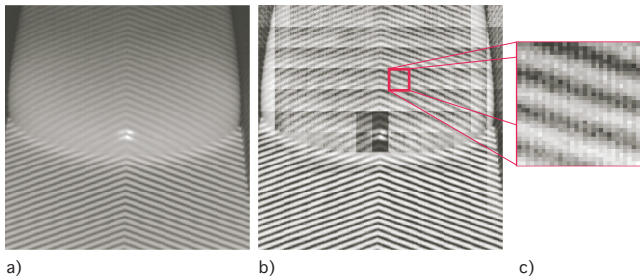


Fig. 12 a) grabbed image, b) local wave retrieval using window, c) close-up of one window.

When this method is used with a symmetric projection [see Fig. 12(a)], special attention should be paid to the calibration procedure as a sudden deviation in the unwrapped phase is likely to appear near the axis of symmetry.

5 Phase unwrapping

Once we have obtained the phase map, we compute the height by unwrapping the phase map. The principle of phase unwrapping is quite easy to understand in one-dimensional problems. Let us consider that we have a phase signal ϕ defined over the interval $[0, 2\pi)$ and we want to unwrap it. Whenever the signal goes out from the interval $[0, 2\pi)$, we add or subtract 2π to it depending on the derivative $\partial_x \phi$, as is shown by Fig. 14.

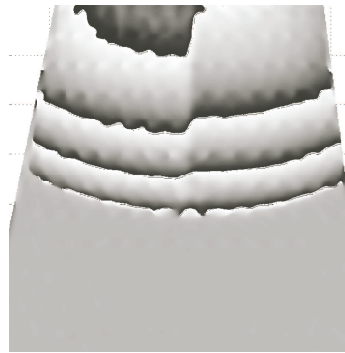


Fig. 13 Phase computed using the local wave retrieval algorithm

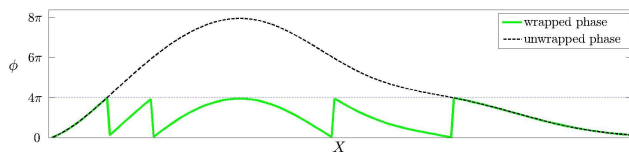


Fig. 14 Example of phase unwrapping in 1D.

Without noise and shadow, phase unwrapping would have a unique solution. Any unwrapping algorithm tends to provide a proper approximate solution. The point is that noise blurs the sharp frontiers of the phase ϕ each time ϕ approaches π (modulo π). Figure 15 shows a typical example of noise disturbance.

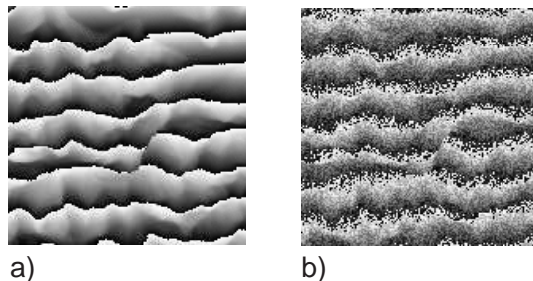


Fig. 15 Phase map: a) original b) with noise

Ideally, to retrieve the phase ϕ from the observed intensity I_k [see Eq. (2)], we would like to have the background intensity A_k equal to zero and the module intensity B_k equal to 255 (for a 8-bit system). In practice, B_k varies between 30 and 120. In order to increase B_k , two solutions are available:

- acquisition time is increased so that more light is received by the camera; or
- the gain of the camera is pushed up to make it more light-sensitive.

In both cases, noise is increased. Indeed, when taking an image, a camera does record the trajectory of

the filmed object. If the displacement is relatively short, the picture looks sharp. In the converse case, if the typical displacement length exceeds one or two pixels, the image is blurred. In the latter case, the reconstructed phase is noisy. In short, we have two alternatives:

- if the acquisition time is long enough, the recorded image is blurred, but the module intensity B_k is relatively high; or
- if the acquisition time is short, the resulting image is sharp, but in the meantime is characterized by lower B_k values.

A tradeoff must be found. To obtain high module intensity B_k while keeping a short acquisition time, we can increase light intensity or increase the gain of the camera. To increase the gain of a CCD camera, the electrical tension at each pixel is increased, so less photons are needed to capture an image.

Shadowed regions appear when the plane surface is not entirely covered by the projected image or when a part of this surface is hidden to the camera, as sketched in Figs. 16 and 17. All the information in the shadowed or hidden parts is lost. In order to high-quality results, one must take care to avoid such regions to take place, while trying to keep the angle between the projecting and acquiring directions as close as possible to 90° . Again, a compromise must be found between the extent of shadowed areas and the incidence-angle mismatch.

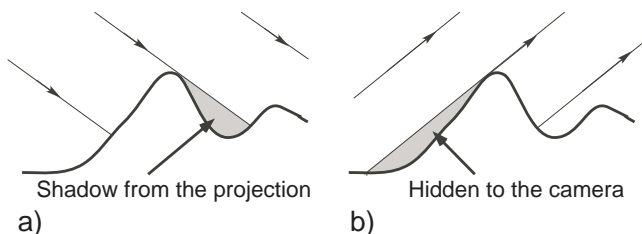


Fig. 16 a) Shadow from the projector, b) hidden parts to the camera

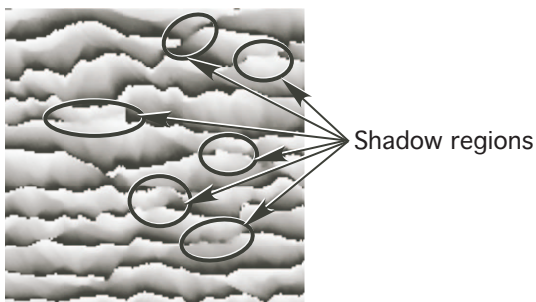


Fig. 17 Shadow regions on an image

To date, different methods can provide approximations to two-dimensional unwrapping problems. Ghiglia and Pritt's book (1998) reviewed different approaches to phase unwrapping. They also provided eight C++ routines illustrating these strategies. On the whole, there are two different approaches to phase unwrapping: one is based on path-following methods or local methods, while the other is based on minimum-norm methods or global methods. The path-following methods starts at a given point in the phase map and computes the neighboring points by following a predefined path. The main difficulty is to choose the best path to avoid shadowed or noisy parts. Minimum-norm methods minimize the integral of the square difference between the gradients of the solution and the path obtained using different strategies. We rank different algorithms by sorting them from the simplest and fastest ones to the more complex and slower ones.

1. Goldstein's branch cut algorithm, *path-following* (Goldstein et al, 1988),
2. Quality-guided algorithm, *path-following*, (Roth, 1995),
3. Unweighted least-squares algorithm, *minimum-norm*,
4. Preconditioned conjugated gradient (PCG) algorithm, *minimum-norm*,
5. Mask-cut algorithm, *path-following*, (Parti et al, 1990),
6. Multigrid algorithm, *minimum-norm*, (Pritt, 1996),
7. Flynn's minimum discontinuity algorithm, *path-following*,
8. Minimum L^p -norm algorithm, *minimum-norm*.

As is usually the case, the best results are not systematically obtained with the most sophisticated algorithms. Even if the last two algorithms turn out to be the most robust ones, it is worth trying them all each time we test a given configuration. After many trials, we opted for Flynn's method because its calculation time is much shorter than the Minimum L^p -norm for nearly equivalent results. Incidentally, note that all these algorithms have tunable parameters, which have not only a large influence on the execution time, but also on the quality of the results.

5.1 Phase difference

A good way to reduce computation time is to unwrap the difference of the two phase maps instead of computing the difference of the respective unwrapped phase, as shown in Fig. 18. The resulting map shows less jumps of 2π , which makes the reconstruction of the unwrapped phase easier, faster, and more accurate. Unwrapping the difference of the object phase map and the reference phase map provides the same results as taking the difference of the unwrapped phases.

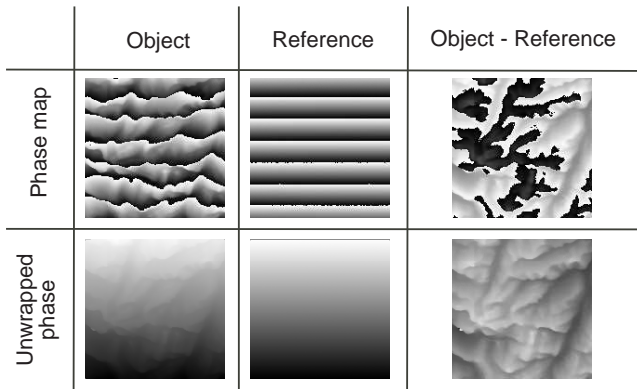


Fig. 18 Unwrapping the difference of the object phase map and the reference phase map is equal to the difference of the unwrapped phases

5.2 Calibration

Equation (1) give the height as a function of the angle α and the distance between two line P_p . Underlying this equation, there is the following assumption: projection and acquisition must be telecentric, which is not the case in our setup (Chen and Quan, 2005). Fig. 19 shows how the angle α between the projection angle and the camera angle varies along the x -axis in a non-telecentric setup; $\alpha_1 \neq \alpha_2$. The same also holds for the projected lines P_p and the apparent line P_a seen by the camera; $P_1 \neq P_2$. A similar figure could be plotted for the y -axis. In principle, knowing the relative position of the camera, the projector, and the inclined plane as well as the projection and camera angles makes it possible to modify Eq (1) by including a height's correction factor for each position (Desmangles, 2003). This method involves accurately measuring the position of each elements of the setup, which it is time-consuming. It does not take optical deformation into account either. For these reasons, we decided to use a more practical calibration procedure, which is based on a modified version of the virtual calibration-plane method proposed by Xiaoling et al (2005).

To calibrate our measurement system, we proceeded as follows:

1. Well-defined patterns such as squares were projected on the inclined plane to adjust the focuses of the projector and camera.
2. We checked that the recorded images from the camera properly included the zone of interest. Light power and projection resolution were optimized by fitting the size of the projected images with the plane size.
3. We related the Cartesian coordinates x, y, z of the plane with a grid i, j , each cell representing a pixel of the unwrapped phase. To that end, we designed a calibration plate, i.e., a simple plane surface, over which we marked gray disks of 2 cm in diameter and spaced apart by 10 cm. The upper surface of this

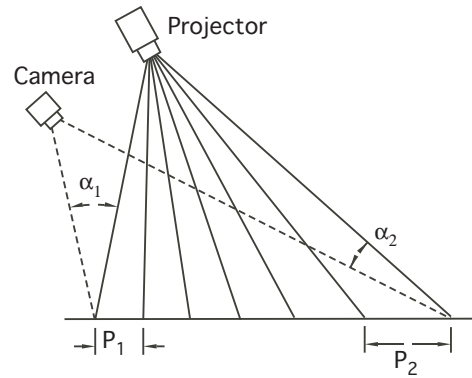


Fig. 19 Variation in the angle α for a non-telecentric setup.

plane corresponded to elevation $z_0 = 0$. All fringe patterns, which were used in each experimental run, were then projected on this calibration plane [see Fig. 20(a)]. The module of the reference plane was computed [see figure 20(b)] and the position of the circle centers were found using a least-square approach [see Fig. 20 (c)].

4. The wrapped phase was referred to as ϕ_{z_0} [see figure 20(d)]. A relation between the plane xy_{z_0} and the camera coordinates ij was obtained using a piecewise linear interpolation.
5. Any circles that was partially contained in the image was removed since its center could not be accurately located (information was partly lost). If it were kept, it would introduce distortion.

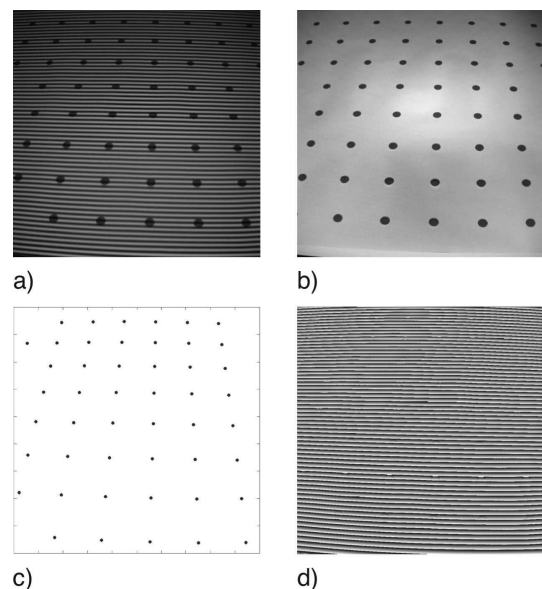


Fig. 20 a) Projection of the fringe on the calibration plate, b) module with the calibration circles, c) position of the circle in the camera pixel coordinates and d) phase map of the calibration plane.

The same procedure was repeated k times with the calibration plate placed over the inclined plane at an elevation z_k , with $k = 1, 2, \dots, K$ (see Fig. 21). A relation between the plane xy_{z_k} ($k = 1, 2, \dots, K$) and the camera coordinates ij was obtained using a piecewise linear interpolation. The corresponding wrapped phase ϕ_{z_k} was computed and the phase difference $\phi_{z_k} - \phi_{z_0}$ was unwrapped and denoted by ψ_{z_k} . Note that ψ_{z_k} is not unique since $\phi_{z_k} - \phi_{z_0} \in [0, 2\pi)$. z_k is a function of $\varphi_{z_k} = \psi_{z_k} + j\pi$, with $j = 1, 2, \dots$. A way of finding j is explained in Sect. 5.2.1. Once $\varphi_{z_k} = \psi_{z_k} + j\pi$ was defined, a piecewise linear interpolation method was used to complete z -axis calibration. The unwrapped phases φ_k ($k = 1, 2, \dots, K$) at elevation z_k ($k = 1, 2, \dots, K$) were considered as reference phases. Based on the reference phases and their elevations z_k , every pixel height (z -axis coordinate) were obtained by linearly interpolating φ_k and z_k .

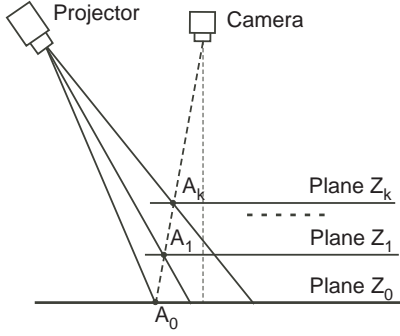


Fig. 21 Calibration with virtual planes z_k .

We ended up with a calibration matrix $M_{ij\phi}$, which related the value of the unwrapped phase φ_k in the pixel coordinate system ij with the elevation z_k in the plane coordinate system xy . Figure 22 shows the matrix $M_{ij\phi}$ with five surfaces φ_k , which represented five different elevations z_k : 5 mm, 25 mm, 45 mm, 65 mm, and 85 mm. The dots represent the position of the circle centers located on the calibration plane.

The steps, which appear in the middle of each surface φ_k , are the consequences of a symmetric projected pattern, which was not aligned with the x - or y -direction of the calibration plane. For the camera, the projection angles on either side of the symmetry axis are different, which leads to contrasted sensitivity to flow depth [see Eq. 1]. A closer look at Fig. 23(a) shows that the axis of symmetry of the projected pattern is not vertical; the angle of projection is slightly different on either side of that line. This leads to a step-shaped variation in the phase map [see Fig. 23(b)] as well as in the unwrapped phase map [see Fig. 23(c)]. As expected, thanks to the calibration process, the resulting surface does not show any step [Fig. 23(d)].

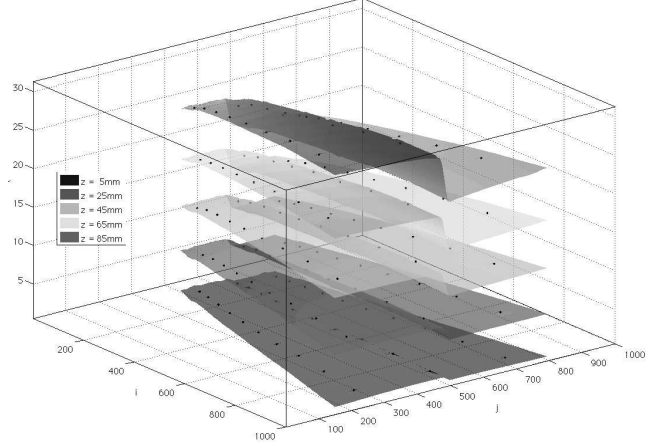


Fig. 22 Calibration matrix $M_{ij\phi}$ with 5 reference planes $z - k$. The dots represent the position of the circle centers on the calibration plane.

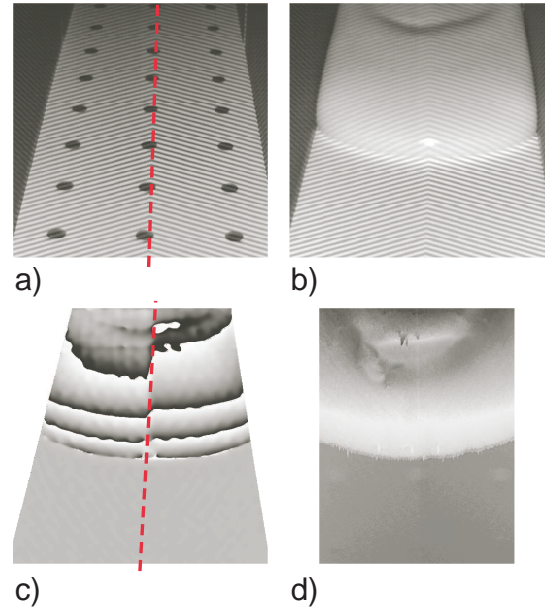


Fig. 23 Projection of a symmetric pattern not aligned with the reference plane, a) grabbed image of the reference plane with the axis of symmetry in dash line, b) grabbed image of the sluice, c) phase map with a step on the axis of symmetry, d) resulting surface without any step.

Compared with classical ways of calibration, this method reduces the hardware requirement of the system. It also simplifies the process of grabbing and processing data. Better accuracy is achieved by increasing the number of virtual calibrating planes z_k . The standard deviation error, using 5 virtual planes, is of the order of 1%.

5.2.1 Temporal phase unwrapping

A problem arose with our setup: two calibration planes with two different heights could yet have the same phase ϕ_{z_k} . To get round this problem, we used temporal phase unwrapping (TPU). Temporal phase unwrapping (TPU) was presented at length by Huntley and Saldner (1997). It involves unwrapping a phase with high sensitivity by means of others phases with lower sensitivity. First, a series of phase-shifted images (see Sect. ??) is projected with a projected lengthwave L_{p_1} that is longer or equal to the surface to be measured. The wrapped phase ϕ_1 is then set equal to the unwrapped phase φ_1 [see Fig. 24(a)]. Height resolution is low. A second series of phase shifted images is projected onto the surface, but with a lengthwave $L_{p_{\frac{1}{2}}}$ set to half the size of L_{p_1} . The wrapped phase $\phi_{\frac{1}{2}}$ is unwrapped by looking up at the wrapped phase φ_1 [see Fig. 24(b)]. This process is repeated n times until the desired $\phi_{\frac{1}{n^2}}$ is reached.

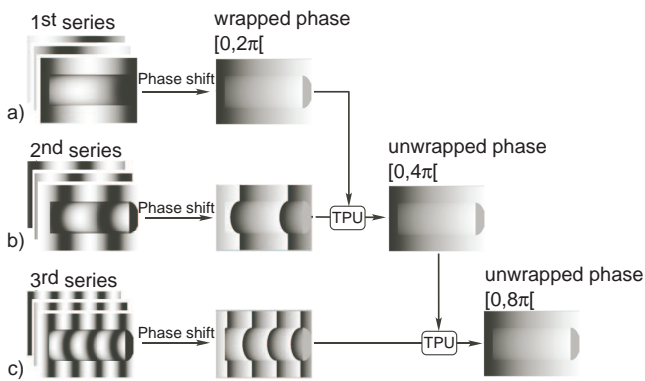


Fig. 24 Temporal phase unwrapping: a) a first series of images with a large length wave, so the wrapped phase is set equal to the unwrapped one, is projected, b) the length wave is divided by 2 and a new series is projected, the unwrapped phase is obtained by looking up at the first unwrapped phase, c) a new series is then projected with a length wave divided again by 2.

5.3 Distributed computing

The mean time spent from acquiring an image to obtaining a three-dimensional surface takes nearly 5 minutes:

- on average, one-image algorithm for retrieving the phase (see Sect. ?? and ?? takes 1'30";
- phase unwrapping takes 1 min (Goldstein) to 1.5 h (L_p -norm), depending on the complexity of the object phase (see Sect. 5);
- phase unwrapping takes 2 min;
- transforming the unwrapped phase map into an image in a Cartesian coordinate system takes about 1.5 min, depending on the number of virtual plane z_k used (see Sect. ??).

Given that a typical experimental test lasts 1 min (usually from 30 s to 2 min) and we operate out camera at 45 fps, we end up with 2'700 images. The total computational time is 225 hours (9.5 days), which would make the method of limited interest when many experiments have to be conducted. In order to speed up calculation, we use the *Distributed Computing Toolbox* from Matlab, with a grid of 21 CPUs, which makes it possible to reduce the computational time to 12 hours.

As shown in Fig. 25, a grid is made up of one client, a controller or job manager, and workers or agents. The client submits a job, composed of many different tasks, to the controller (1). The controller distributes the different tasks to the agents (2). The agents then execute the tasks (3). The main difference between a grid and a cluster is that agents, in a grid, do not exchange information when doing their job. Once the task executed, the agents return the outcome to the controller (4). Once all the tasks completed, the controller returns the final outcome to the client. Many clients can submit jobs to the controller, which then dispatches the tasks to the available agents. Agents can be dedicated to the grid and always be accessible by the controller or not. In the latter case, the agent is a personal computer, which becomes available to the grid only when its user is not there, e.g., by night or during the week end.

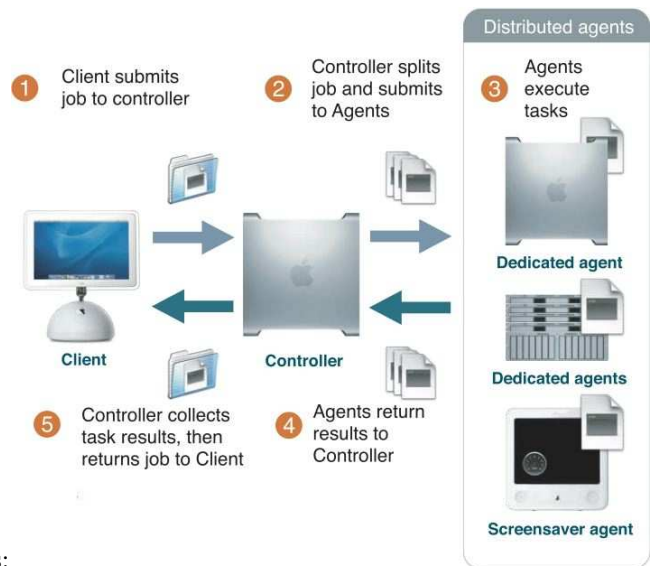


Fig. 25 Distributed computing grid

A grid is usually built on a normal network infrastructure in order to minimize data transfer and increase the mean duration of individual job. Creating a unique task for retrieving the phase from the acquired images, unwrapping it, and transforming it in a Cartesian coordinate system, saves more time than splitting the task into several subtasks.

6 Example

Here, we provide the results that we obtained when unleashing a 60-l volume of Carbopol Ultrez 10 at a solid concentration of 0.3% down a 30-cm wide channel. The bed inclination was 15° with respect to the horizontal and the channel cross-section was rectangular.

Figure 26(a) represents the grabbed image of the flow taken at time $t_1 = 0.68$ s. The wrapped phase was obtained by a local wave retrieval algorithm. The unwrapped phase was computed using the “quality-guided” algorithm. The final height was obtained using the same calibration matrix as that shown in Fig. 22.

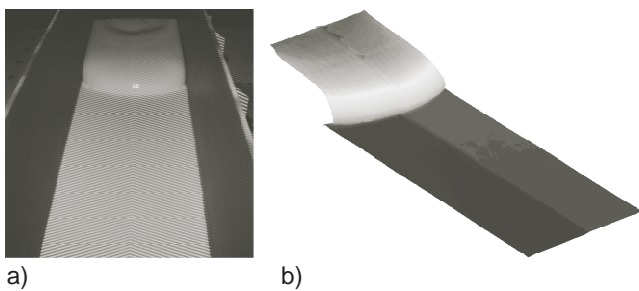


Fig. 26 Free surface at $t_2 = 0.68$ s: a) 1 image used for the local wave retrieval algorithm, b) the free surface height.

For the same run but, Fig. 27 provides a snapshot at $t_2 = 2.05$ s. Because the flow slowed down, a 3-image phase-shift algorithm was used. Figure 27(a) shows the three images used to calculate the wrapped phase. The wrapped phase was still computed using the “quality-guided” method. The height is shown in Fig. 27(b).

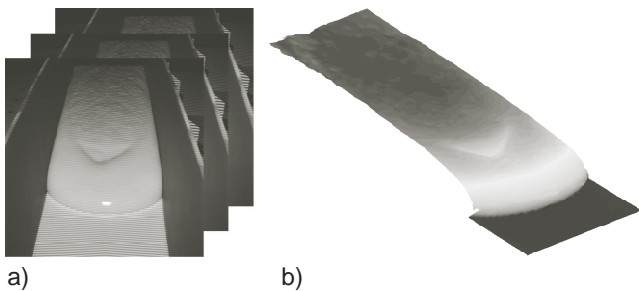


Fig. 27 Free surface at $t_2 = 2.05$ s: a) 43 images used for the phase-shift algorithm, b) the free surface height.

7 Conclusion

New experimental facilities and procedures have been built to accurately measure the three-dimensional flow depth profiles in the dam-break problem. A mass of viscoplastic fluid is suddenly released by opening the dam

sluice gate down a 4.5 m long inclined plane. The three-dimensional flow-depth profiles are measured using a high-speed digital camera, which records how a fringe pattern projected onto the flow surface is deformed. To ensure uniform projection, a micro-mirror projector is used. The projector and the camera are synchronized at 48 Hz.

A cosine fringe pattern is projected onto the surface by the micro-mirror projector. A wrapped phase, from the recorded deformed images, is obtained using a 3-4 images phase shift algorithm or using a single image with Fourier transformation profilometry (FTP) or a local wave retrieval algorithm. The wrapped phase is then unwrapped using algorithms proposed by Ghiglia and Pritt (1998). The quality of the unwrapping algorithm depends on many parameters, which are user-dependent. Flynn’s algorithm (Flynn, 1997) tends to give the best time/accuracy ratio.

Height can be related to the unwrapped phase by a calibration matrix. The calibration matrix is obtained by placing a calibration plate at different elevation z_k and relating the pixel coordinates ij with circles on the plane to get the XY coordinates. At the same time, the phase of each z_k plane is recorded.

The 3-4 images phase-shifting method is used when the distance travelled by the surge is lower than one or two pixels between the first and the last image. Local wave retrieval algorithm is preferred when the flow is fast because only one image is needed.

Even though we are still improving the procedure to reduce the dependency of the results on the user, we are quite confident of the method expounded in this paper. The characteristics of the flow down the inclined plane (e.g., flow depth profile, front velocity) can be related with its rheological properties. The precision on the surface height is of the order of 0.1 mm for a surface of 1.8×1.2 m².

References

- Bartelt P, Salm B, Gruber U (1999) Calculating dense-snow avalanche runout using a Voellmy-fluid model with active/passive longitudinal straining. *J Glaciol* 45:242–254
- Chen L, Quan C (2005) Fringe projection profilometry with nonparallel illumination: a least-squares approach. *Optics Letter* 30(16):2101–2103
- Desmangles AI (2003) Extension of the fringe projection method to large objects for shape and deformation measurement. PhD thesis, EPFL
- Flynn T (1997) Two-dimensional phase unwrapping with minimum weighted discontinuity. *Journal of the Optical Society of America* 14(10):2692–2701
- Ghiglia DC, Pritt MP (1998) Two-dimensional phase unwrapping: theory, algorithms, and software. Wiley-Interscience, Wiley, cop.

- Goldstein R, Zebker H, Werner C (1988) Satellite radar interferometry: two-dimensional phase unwrapping. *Radio Science* 23(4):713–720
- Griffiths R (2000) The dynamics of lava flows. *Annu Rev Fluid Mech* 32:477–518
- Hogg A, Pritchard D (2004) The effects of hydraulic resistance on dam-break and other shallow inertial flows. *J Fluid Mech* 501:179–212
- Huang X, Garcia M (1997) A perturbation solution for Bingham-plastic mudflows. *Journal of Hydraulic Engineering* 123:986–994
- Huntley JM, Saldner HO (1997) Shape measurement by temporal phase unwrapping: comparison of unwrapping algorithms. *Meas Sci Technol* 8:989–992
- Iverson R (1997) The physics of debris flows. *Rev Geophys* 35:245–296
- Iverson R, Logan M, Denlinger R (2004) Granular avalanches across irregular three-dimensional terrain: 2. Experimental tests. *J Geophys Res* 109:F01,015
- Jeong MS, Kim SW (2002) Color grating projection moire with time-integral fringe capturing for high-speed 3-D imaging. *Opt Eng* 41(8):1912–1917
- Kraus K, Waldhäusl P (1997) *Manuel de photogrammétrie, principes et procédés fondamentaux*. Hermes
- Liebling M, Blu T, Unser M (2004) Complex-wave retrieval from a single off-axis hologram. *J Opt Soc Am A* 21(3):367–377
- Niclass C, Rochas A, Besse P, Charbon E (2005) Design and Characterization of A CMOS 3D Image Sensor based on Single Photon Avalanche Diodes. *Journal of Solid-State Circuits* pp 1847–1854
- Parker G, Fukushima Y, Pantin H (1986) Self-accelerating turbidity currents. *J Fluid Mech* 171:145–181
- Parti C, Giani M, Leuratti N (1990) SAR interferometry: A 2-D phase unwrapping technique based on phase and absolute values information. In: IEEE N Piscataway (ed) *International Geoscience and Remote Sensing Symposium*, pp 2043–2046
- Pritchard D (2005) On fine sediment transport by a flood surge. *J Fluid Mech* 534:239–248
- Pritt M (1996) Phase unwrapping by means of multigrad techniques for interferometric SAR. *IEEE Transactions on Geoscience and Remote Sensing* 34(3):728–738
- Ritter A (1892) *Die Fortpflanzung der Wasserwellen*. *Zeit Vereines Deutsch Ing* 36(33):947–954
- Roth M (1995) Phase unwrapping for interferometric SAR by the least-error path. Tech. rep., Johns Hopkins University Applied Physics Lab Technical Report
- Saint Venant B (1871) *Théorie du mouvement non permanent des eaux, avec application aux crues des rivières et à l'introduction des marées dans leur lit*. *C R Acad Sci Paris sér I* 173:147–154– 237–240
- Sansoni G, Carocci M, Rodella R (1999) Three-dimensional vision based on a combination of gray-code and phase-shift light projection: analysis and compensation of the systematic errors. *Appl Optics* 38:6565–6573
- Su X, Chen W (2001) Fourier transform profilometry: a review. *Optics and Lasers in Engineering* 35:263–284
- Takeda M, Ina H, Kobayashi S (1982) Fourier-transform method of fringe-pattern analysis for computer-based topography and interferometry. *Journal of the Optical Society of America* 72(1):156 – 160
- Xiaoling Z, Yuchi L, Meirong Z, Xiaobing N, Yinguo H (2005) Calibration of a fringe projection profilometry system using virtual phase calibrating model planes. *J Opt A: Pure Appl Opt* 7:192–197
- Author, Article title, Journal, Volume, page numbers (year)